(Received 6 February 2026, Accepted 9 April 2026, Scheduled 19 May 2026)

Frequency-Tunable and Attenuation-Controlled Sub-6 GHz Antenna Using Miniaturized Multilayer Graphene Pads

Pandillapalli Janardhana Reddy[1,*] and Gummadi Kameswari[2]

[1] *Department of ECE, RGUKT-AP, R K Valley Campus, Research Scholar JNTUA, India*
[2] *Department of ECE, NBKR Institute of Science and Technology, Tirupati, India*

ABSTRACT: This paper presents a wideband four-port microstrip antenna operating from 2.75 GHz to 6.75 GHz with frequency reconfigurability and controllable notch characteristics. The antenna employs an asymmetric radiating structure to realize circular polarization around 5.5 GHz, while multilayer graphene (MLG) pads are introduced to enable bias-controlled frequency tuning and adjustable band rejection. The four-port configuration, implemented on an RT/Duroid 5880 substrate ($\varepsilon_r = 2.2$, thickness $= 1.6$ mm), achieves inter-element isolation better than 20 dB without additional decoupling structures. The proposed design also exhibits strong diversity performance with an envelope correlation coefficient below 0.02 and diversity gain above 9.97 dB. The results demonstrate that the proposed antenna provides a compact and low-complexity solution for wideband and reconfigurable sub-6 GHz wireless communication applications.

1. INTRODUCTION

Tunable and reconfigurable antennas have become essential for modern wireless communication systems because of their ability to efficiently utilize the limited frequency spectrum. Unlike conventional antennas with fixed operating characteristics, tunable antennas can dynamically modify their operating frequency, radiation pattern, or polarization in real time [1–3]. However, achieving reconfigurability introduces several design challenges, including impedance matching, radiation stability, and gain preservation, which require careful investigation [4].

Various techniques have been reported to realize antenna reconfigurability, including PIN diodes, varactor diodes, micro-electromechanical switches (MEMSs), photoconductive switches, liquid crystals, liquid metals, mechanical tuning, and other adaptive materials [5]. Metallic posts placed along orthogonal axes enable independent frequency tuning and circular polarization through dimensional variation of perturbing elements [6]. Frequency-agile microstrip antennas employing varactor-loaded circular patches connected to annular rings have demonstrated frequency tuning capability [7]. Other reported structures include truncated circular radiators with parasitic elements, compound unit-cell antennas loaded with PIN diodes, and orthohexagonal patch antennas incorporating parasitic patches and varactors for simultaneous frequency and polarization reconfiguration [8, 9]. Field programmable gate array (FPGA)-controlled antennas using switchable feeding ports and lumped capacitors have also been explored for tunable operation [10]. Pixel-based parasitic surfaces with multiple PIN diodes enable multifunctional reconfigurability, including frequency tuning, beam steering, and polarization switching [11]. In addition, liquid-metal-based reconfigurable apertures embedded in elastomeric substrates have demonstrated continuous frequency tuning over a wide operating range [12].

Tunability has also been extended beyond antennas to include microwave components, such as diplexers and filters. Varactor and PIN diode-based tunable diplexers with independently controlled channels have been reported, offering wide tuning capability and stable return loss characteristics [13, 14].

Recently, graphene has attracted significant attention for microwave and radio frequency (RF) applications owing to its electrically tunable surface conductivity. Initially investigated at terahertz frequencies, graphene has progressively been investigated for microwave-band devices. Its unique linear energy-momentum dispersion and low-energy Fermi level modulation enable conductivity control through external biasing [15]. Graphene-integrated tunable attenuators, filters, power dividers, antennas, and absorbers have been demonstrated, highlighting its suitability for adaptive microwave systems [16–20]. In particular, graphene has been employed as a tunable lossy element in bandpass duplexers, where bias-controlled sheet resistance enables adjustable attenuation by absorbing concentrated electric fields [21–24]. Furthermore, antennas incorporating graphene-based switches placed along slotted radiators have achieved reconfigurability by modulating the surface conductivity, thereby enabling dynamic control of the amplitude and phase characteristics [25, 26].

Despite these developments, most reported tunable antennas rely on multiple active components, such as varactor diodes, PIN diodes, MEMSs, and photoconductive switches, resulting in increased circuit complexity, biasing requirements, and power consumption. For instance, the designs reported in [13] and [14] employ a large number of varactor diodes, leading to

* Corresponding author: Pandillapalli Janardhana Reddy (janardhanareddypandillapalli@gmail.com).

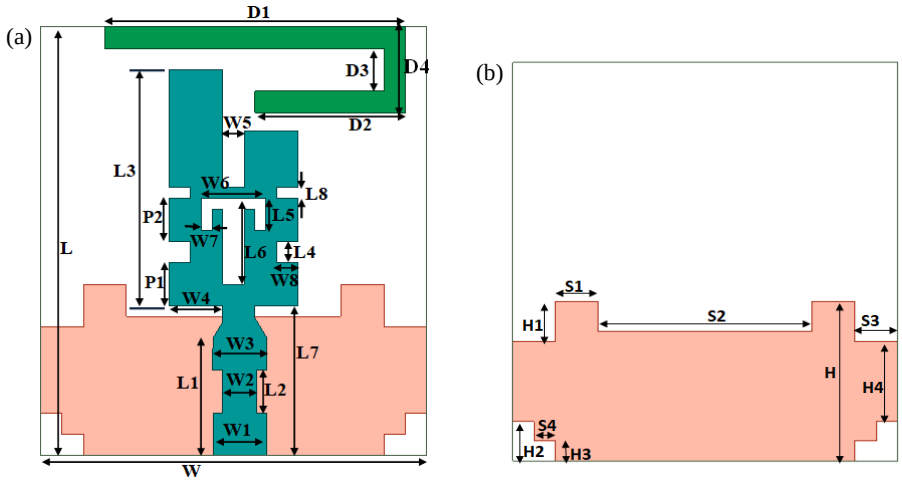

FIGURE 1. Geometry of the proposed antenna: (a) Front view and (b) back view.

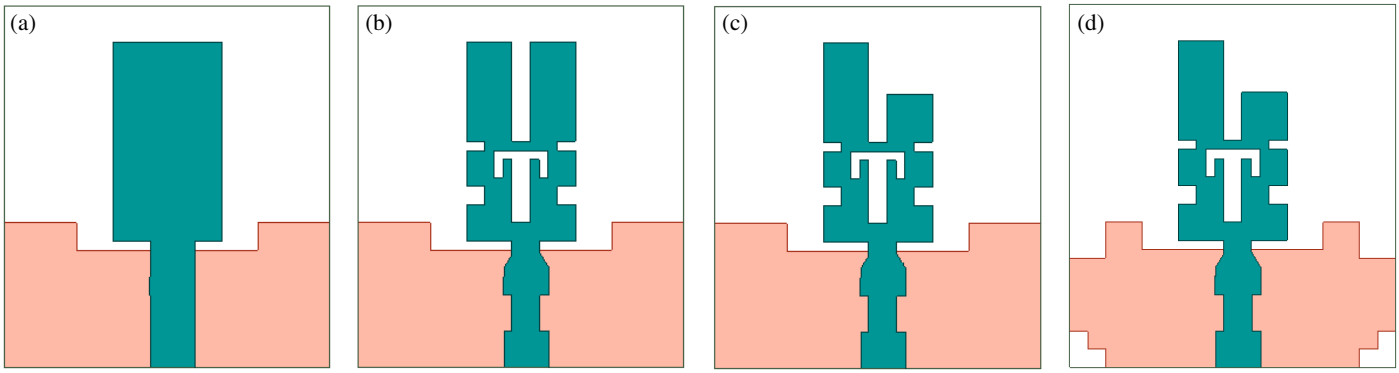

FIGURE 2. Optimization process of the antenna. (a) Phase-1, (b) Phase-2, (c) Phase-3, (d) Phase-4.

complex biasing networks and bulky implementations. The extensive use of active components also increases implementation difficulty and may affect the overall system reliability.

To address these limitations, the proposed design employs compact multilayer graphene pads with controllable resistance to achieve frequency tunability and adjustable attenuation. The reduced pad size minimizes surface resistance and insertion losses compared with previously reported graphene-based implementations. Moreover, the simplified architecture and straightforward biasing scheme enable low-power operation while maintaining effective tunable performance. These features make the proposed antenna suitable for compact and adaptive sub-6 GHz wireless communication systems.

The organization of this manuscript is as follows. Section 2 presents the optimized antenna design procedure. Section 3 discusses the fabrication and incorporation of multilayer graphene pads. Section 4 validates the simulation results through measurements. Finally, Section 5 summarizes the work.

2. ANTENNA GEOMETRY AND DESIGN

The proposed antenna was developed on an RT/Duroid 5880 substrate with a thickness of 1.6 mm and physical dimensions of $18 \times 20\,\text{mm}^2$. Figures 1(a) and 1(b) illustrate the front and back views of the antenna structure, which was excited using a half-wavelength ($\lambda/2$) feed line. The optimized design parameters of the antenna are summarized in Table 1.

TABLE 1. Geometrical parameters of the proposed single antenna.

Parameter	W	L	$W1$	$W2$	$W3$	$W4$
Values (mm)	18	20	2.5	1.5	2.5	2.5
Parameter	$W5$	$W6$	$W7$	$W8$	$L1$	$L2$
Values (mm)	1	3	0.5	1	5.5	2
Parameter	$L3$	$L4$	$L5$	$L6$	$L7$	$L8$
Values (mm)	11	1	1.5	3.5	7	0.5
Parameter	$P1$	$P2$	$S1$	$S2$	$S3$	$S4$
Values (mm)	2	2	2	10	2	1
Parameter	$H2$	$H3$	H	$H1$	$H4$	$D1$
Values (mm)	2	1	8	2	4	14
Parameter	$D2$	$D3$	$D4$			
Values (mm)	7	2	4			

Figure 2 shows the antenna optimization process and the corresponding simulated results for each step shown in Figure 3.

The initial antenna, Phase-1, comprises a rectangular patch with a 50 Ω microstrip feed, as shown in Figure 2(a), and oper-

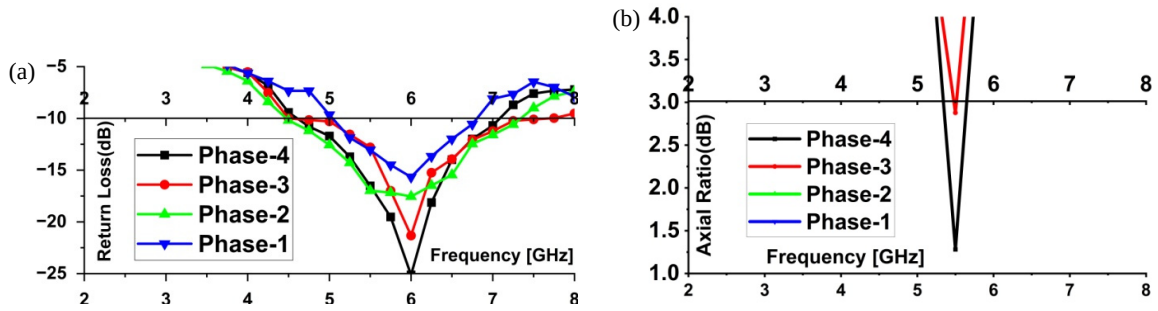

FIGURE 3. Simulated results. (a) S_{11} parameter. (b) Axial ratio.

ates over 5 GHz–7.67 GHz (Figure 3(a)). The analytical formulation of the proposed antenna is based on classical microstrip transmission-line theory combined with the fringing-field correction models. The resonant arm of the radiator uses an effective patch width of 6 mm and a physical length of $L3 = 11$ mm, placed on an RT/Duroid 5880 substrate with $\varepsilon_r = 2.2$ and $h = 1.6$ mm. The corresponding effective dielectric constant is obtained from the standard microstrip approximation as given in Eq. (1).

$$\varepsilon_{eff(patch)} = \frac{\varepsilon_r + 1}{2} + \frac{\varepsilon_r - 1}{2} \frac{1}{\sqrt{1 + 12\left(\frac{h}{w}\right)}} \approx 1.893 \quad (1)$$

The electrical length is further increased by the fringing fields, computed using the Hammerstad extension model, as given in Eq. (2).

$$\Delta L_{patch} = 0.412h \frac{(\varepsilon_{eff} + 0.3)\left(\frac{w_p}{h} + 0.264\right)}{(\varepsilon_{eff} - 0.258)\left(\frac{w_p}{h} + 0.8\right)} \approx 0.779 \quad (2)$$

A similar analysis is applied to the feed strip with a width of 2.5 mm and length of 6 mm, for which the effective permittivity and fringing extension are found to be $\varepsilon_{eff,feed} \approx 1.803$ and $\Delta_{feed} \approx 0.69$ mm, respectively. The dominant resonant current path in Phase-1 is formed by the combined length of the radiating arm and the feed, providing a total physical path of the antenna $L3 + L_{feed} = 11 + 6 = 17$ mm. Because these two sections support different field distributions, an averaged effective permittivity of $\varepsilon_{eff,avg} = \frac{1.893+1.803}{2} = 1.848$ and an averaged fringing extension of $\Delta L_{avg} = \frac{0.779+0.69}{2} = 0.7345$ mm are adopted for a first-order approximation. The resulting effective electrical length obtained using Eq. (3) is

$$L_{eff} = (L3 + L_{feed}) + 2\Delta L_{avg} = 18.469\,\text{mm} \quad (3)$$

Using the half-wavelength open resonator model, the fundamental resonance frequency is predicted using Eq. (4).

$$f_r = \frac{c}{L_{eff}\sqrt{\varepsilon_{eff}}} \approx 5.68\,\text{GHz} \quad (4)$$

which aligns well with the simulated value of 6 GHz. This confirms that the analytical formulation accurately captures the resonant behavior of the antenna in Phase-1.

In Phase-2, as shown in Figure 2(b), a folded T-shaped slot ($W5 = 1$ mm, $W6 = 3$ mm, $L5 = 1.5$ mm) is etched into the radiating patch, perturbing the surface-current distribution. The slot interrupts the dominant current path and forces current detouring, reducing the effective electrical length to approximately $L_{eff} = 8.28$ mm and improving the impedance performance across the operating band, as illustrated in Figure 3(a).

In Phase-3, as depicted in Figure 2(c), an asymmetric cut [28] of 2.85×2.5 mm^2 is introduced on one radiating arm, which breaks the structural symmetry [27] and alters the surface current distribution. This perturbation lifts the degeneracy of the orthogonal resonant modes [29] originally occurring near the fundamental frequency, resulting in mode splitting. The split modes can be expressed [31] as $fx = fr - \Delta f1$ and $fy = fr + \Delta f2$, where the frequency shifts depend on the perturbation introduced by the asymmetric cut. The frequency deviation (Δf) is estimated [32] using the first-order perturbation relation Eq. (5)

$$\frac{\Delta f}{f_r} = \frac{\Delta L}{L} \quad (5)$$

where $\Delta L \approx 2.5$ mm represents the effective perturbation introduced by the asymmetric cut, and $L3 = 11$ mm is the effective resonant length. This yields a frequency shift of approximately $\Delta f \approx 1.36$ GHz. The circular polarization frequency is therefore given by Eq. (6)

$$f_{CP} = \frac{f_x + f_y}{2} \quad (6)$$

which results in $f_{CP} \approx 5.2$ GHz, closely matching the observed circular polarization around 5.5 GHz as shown in Figure 3(b). The superposition of these closely spaced orthogonal modes produces equal field magnitudes with a quadrature phase relationship, satisfying $|Ex| \approx |Ey|$ and $\Delta\phi \approx \pm 90°$.

In Phase-4, as shown in Figure 2(d), a shallow ground corner slot and a folded L-shaped parasitic element introduce a small admittance perturbation that smooths the feed-ground interface. This reduces impedance transitions, lowers local Q-factors, and stabilizes the axial ratio without affecting the fundamental frequency. Combined with the Phase-3 asymmetry, this improves circular polarization stability around 5.5 GHz, as illustrated in Figure 3(b).

2.1. Equivalent Circuit

The equivalent circuit in Figure 4 illustrates the impedance behavior of the proposed antenna. The equivalent-circuit pa-

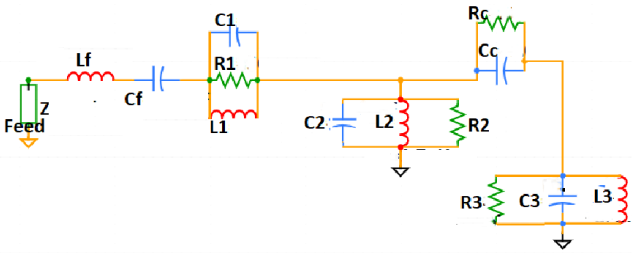

FIGURE 4. RLC equivalent circuit for the proposed design.

rameters for the proposed antenna were extracted using standard transmission-line and resonant-mode formulations widely adopted in microwave engineering. For each resonant branch, the target resonant frequency f_r and quality factor Q_r were related through the classical RLC resonance relations obtained using Eqs. (7) and (8).

$$f_r = \frac{1}{2\pi\sqrt{\mathrm{LC}}} \tag{7}$$

$$Q_r = \frac{f_r}{\mathrm{B.W}} \tag{8}$$

as described [30] and in the RLC antenna models presented by Balanis [31] and Garg et al. [32]. Using the chosen series loss resistance $R \approx 50\,\Omega$, the modal inductance and capacitance were computed using Eqs. (9) and (10).

$$L = \frac{QR}{W_r} \tag{9}$$

$$C = \frac{1}{W_r^2 L} \tag{10}$$

following the S-parameter-based equivalent-circuit extraction approach of Amari et al. [33]. For the feed line, a 6-mm microstrip section on RT/Duroid 5880 ($\varepsilon_r = 2.2$) was modeled as a quasi-TEM transmission line. The effective dielectric constant $\varepsilon_{eff} \approx 1.8$ and propagation velocity predicted using Eq. (11).

$$V = \frac{C}{\sqrt{\varepsilon_{eff}}} = 2.24 \times 10^8\,\mathrm{m/s} \tag{11}$$

were determined using the Hammerstad-Jensen microstrip model [34]. For a lossless line, unit length inductance and capacitance are derived using Eq. (12) and Eq. (13).

$$L = \frac{Z_o}{V} \tag{12}$$

$$C = \frac{1}{VZ_o} \tag{13}$$

This is a standard result from microstrip transmission-line theory [30, 35]. Multiplying the inductance and capacitance per unit length by the 6-mm feed length yields the total feed inductance and capacitance, expressed as

$$Lf = L * l\,(\text{length of feed}) = 1.34\,\mathrm{nH/m} \tag{14}$$

$$Cf = l\,(\text{length of feed}) = 0.53\,\mathrm{pF} \tag{15}$$

Applying the above relations to the observed resonances in Phase-4, the extracted R, L, C values are listed in Table 2.

The coupling branch (Rc, Cc) follows the slot-coupled resonator modeling used in Hong and Lancaster's filter theory [36] and the notch-band circuit models for ultra-wideband (UWB) antennas in [37, 38] by Mandal et al. and Lee et al.

In Phase-1, the antenna consists of a single radiating patch supporting a dominant surface current path, producing a fundamental resonance at approximately 6 GHz. This behavior is modeled by the first RLC branch ($R1, L1, C1$).

In Phases 2 and 3, the introduction of a folded T-shaped slot and asymmetric modification alters the effective electrical length and introduces additional current paths, improving impedance matching. These effects are represented by additional parallel RLC branches ($R2, L2, C2$) and ($R3, L3, C3$), respectively, with coupling modeled by Rc and Cc. The proposed equivalent circuit is validated through the close agreement between the advanced design system (ADS) circuit results and full-wave simulations.

The Smith chart obtained from the ADS equivalent circuit in Figure 5, based on the transmission line model parameters, shows a similar impedance trend to the High Frequency Structure Simulator (HFSS) results with minor deviations at lower frequencies owing to modeling simplifications.

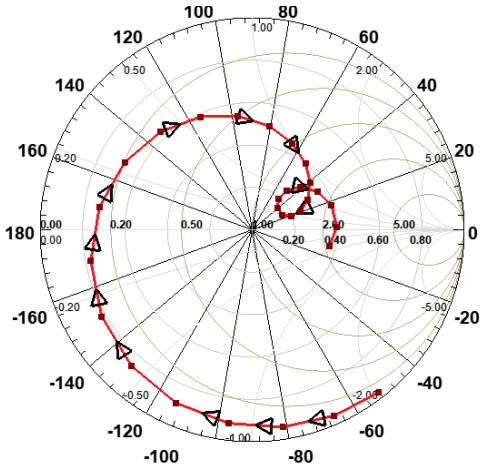

FIGURE 5. ADS impedance matching verification.

3. IMPLEMENTATION OF MLG PADS

Multilayer graphene (MLG) pads are strategically integrated along the asymmetric edges of the radiating patch to facilitate tunable operation. Due to graphene's linear energy-momentum dispersion near the Dirac point, its surface conductivity can be effectively controlled by adjusting the Fermi level through external biasing. By varying the sheet resistance of the MLG, the surface current distribution and input impedance are modified, thereby altering the electromagnetic coupling between the radiating patch and parasitic element. This mechanism enables frequency tunability and reconfigurable antenna performance. To obtain the desired tuning characteristics, the dimensions of the graphene pads are optimized to $1 \times 2.5\,\mathrm{mm}^2$ for MLG-1

TABLE 2. Extracted RLC parameters for the resonance modes observed in Phase-4.

Element	Role/Mode	Value (approx.)
Lf	50 Ω microstrip feed (6 mm)	1.34 nH
Cf	Feed distributed capacitance	0.53 pF
$R1$	Fundamental mode loss (∼6 GHz)	50 Ω
$L1$	Fundamental inductance	4.0 nH
$C1$	Fundamental capacitance	0.18 pF
$R2$	Loss due to slot	50 Ω
$L2$	Inductance due to slot	1.77 nH
$C2$	Capacitance due to slot	0.079 pF
$R3$	Loss due to asymmetric cut and parasitic element	50 Ω
$L3$	Inductance due to asymmetric cut and parasitic element	1.40 nH
$C3$	Capacitance due to asymmetric cut and parasitic element	0.062 pF
Rc	Coupling/notch loss	200 Ω
Cc	Coupling/notch capacitance	0.02 pF

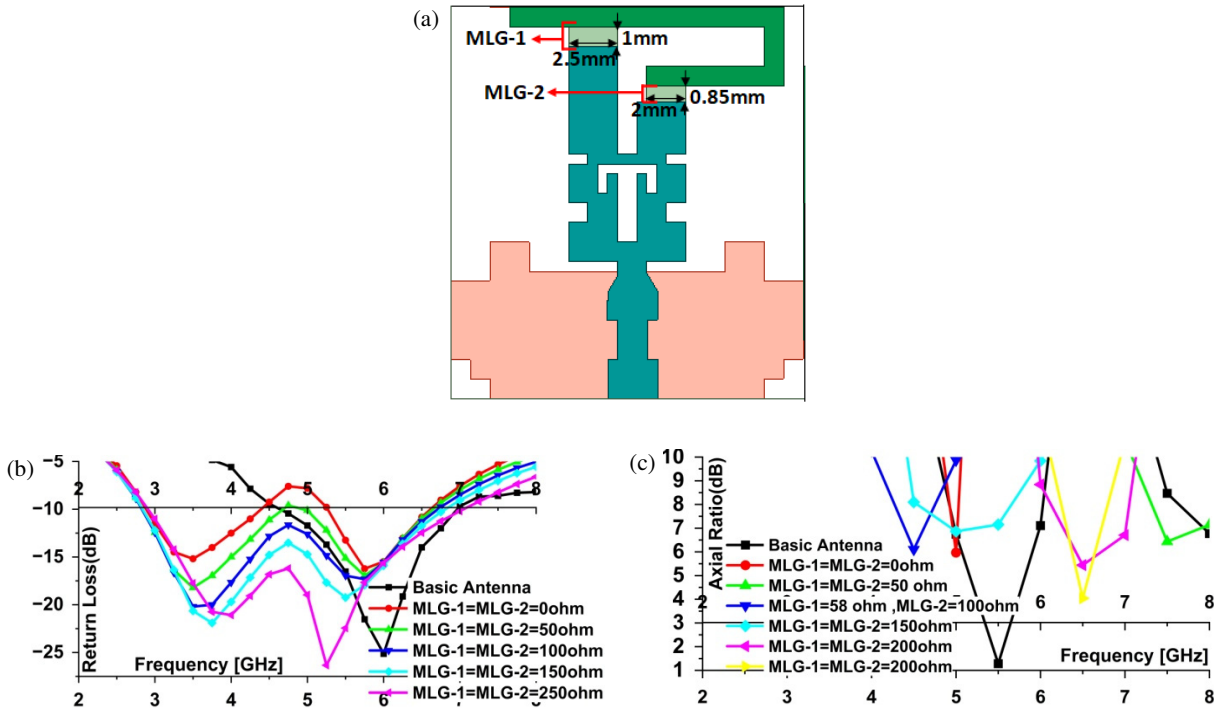

FIGURE 6. Configuration of the proposed MLG-based tunable antenna. (a) The schematic with integrated graphene pads. (b) Return loss characteristics. (c) Axial ratio characteristics.

and $0.85 \times 2\,\text{mm}^2$ for MLG-2. The top view of the antenna and its corresponding responses under different graphene resistance states are presented in Figures 6(a) and 6(b).

Furthermore, as shown in Figure 6(c), the introduction of graphene pads perturbs the degeneracy between orthogonal resonant modes, leading to degradation in axial ratio performance. Consequently, the circularly polarized mode at 5.5 GHz is suppressed in the graphene-loaded configuration, indicating a trade-off between circular polarization and frequency tunability.

3.1. Development and Deposition of MLG Pads

High-purity, commercially sourced multilayer graphene (MLG) with flake sizes of 1–5 µm is used to form the graphene pads. To achieve a stable and homogeneous dispersion, the MLG powder is mixed with isopropyl alcohol (IPA) at a concentration of 10 mg/mL and ultrasonicated for 30 min. The resulting suspension is deposited at the interface between the asymmetric radiating patch and the parasitic element using a controlled drop-casting technique, as shown in Figures 7(a) and 7(b).

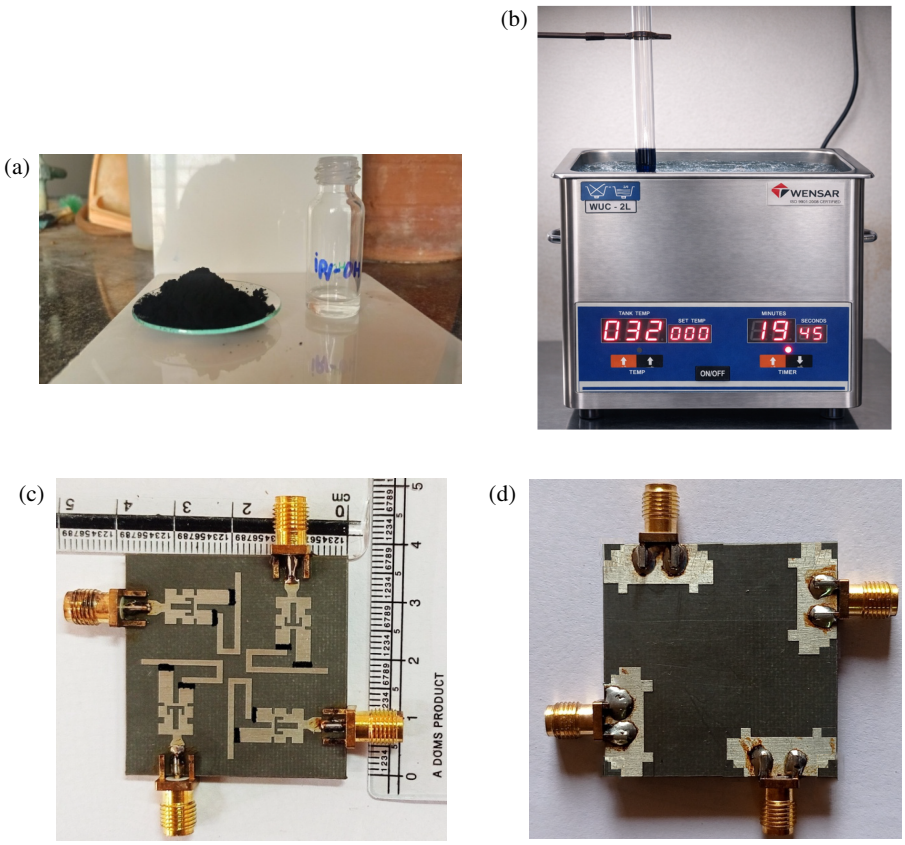

FIGURE 7. (a) Multilayer graphene powder and isopropyl alcohol. (b) Ultrasonic agitation by sonicator. (c) Top view of the fabricated antenna. (d) Bottom view of the fabricated antenna.

This drop-casting method provides a simple and cost-effective fabrication method with acceptable repeatability. After deposition, the IPA evaporates at room temperature, forming a thin multilayer graphene film that acts as a resistive sheet. The deposited graphene exhibits stable and controllable sheet resistance, enabling consistent and reliable tunable performance.

To investigate the effect of graphene resistance variation, multiple antenna prototypes are typically required. In this work, a four-port multiple-input multiple-output (MIMO) antenna configuration is adopted to avoid multiple fabrications. The antenna elements are arranged diagonally within a $38 \times 38\,\text{mm}^2$ area to achieve sufficient isolation, as shown in Figures 7(c) and 7(d). This approach enables efficient evaluation of impedance tuning under different resistance states, while also allowing the analysis of inter-element coupling and isolation in closely spaced configurations.

3.2. Bias-Controlled Electrical Characterization of Graphene Pads

The deposited graphene pads exhibit an initial resistance of approximately $250\,\Omega$ for the selected dimensions. A variable DC bias, as shown in Figure 8, is used to modulate the resistance. The electrical characteristics in Figure 9(a) present the measured I-V behavior and corresponding resistance variation.

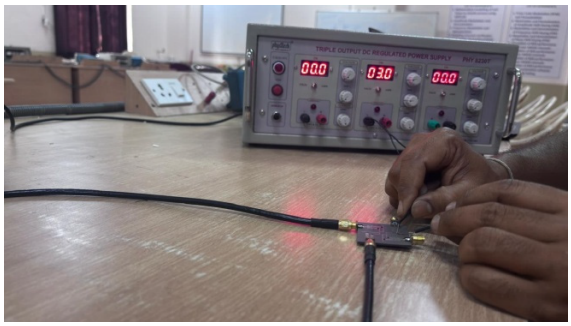

FIGURE 8. Test setup of proposed antenna with graphene pads.

Electrical failure is observed when the bias exceeds 6 V due to material breakdown.

The graphene pads provide resistive tuning with minimal bias current and very low power consumption. This is because the electrical characteristics of multilayer graphene allow resistance modulation through carrier density variation under applied DC bias, rather than through forward current conduction. Unlike semiconductor diodes, graphene behaves as a voltage-controlled resistive sheet with relatively high resistance, and therefore, only a small bias current flows during operation. Consequently, the required biasing power remains very low. In contrast, PIN diodes require continuous forward-bias

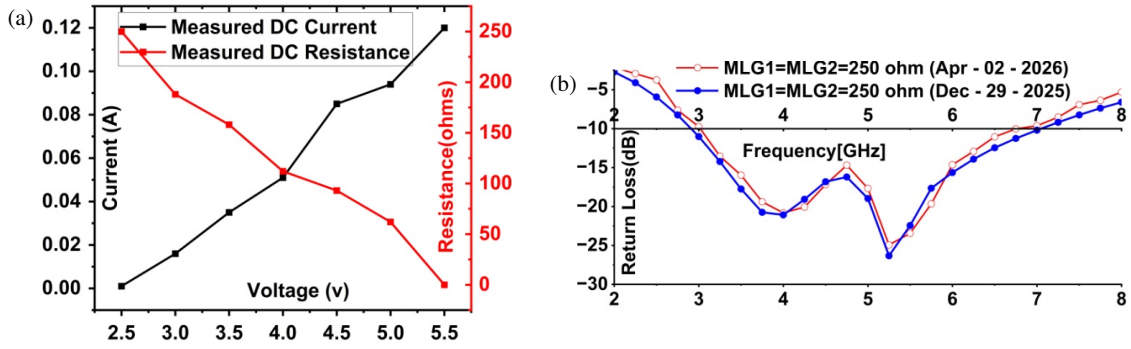

FIGURE 9. (a) Experimental current-voltage behavior and corresponding resistance variation of the MLG pad. (b) Repeatability of measured return loss for MLG pads at two different time intervals.

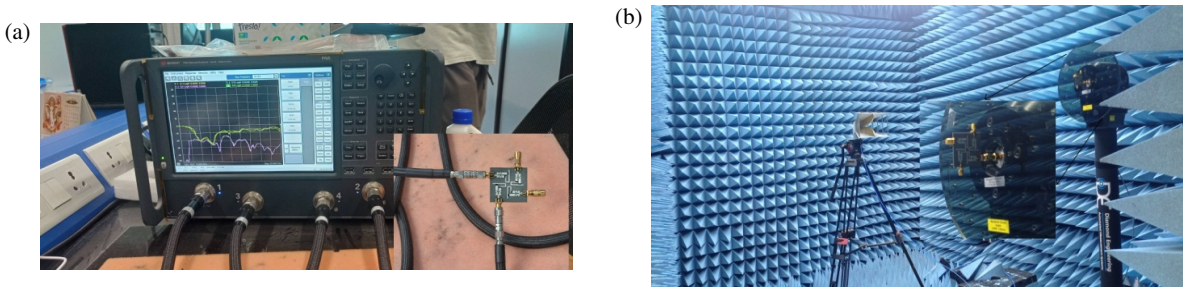

FIGURE 10. (a) S-parameters measurement using vector network analyzer. (b) Radiation characteristics measurement using an anechoic chamber.

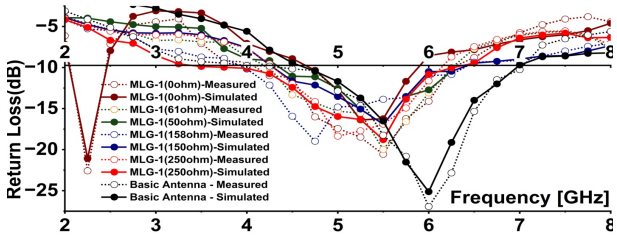

FIGURE 11. Simulated and measured S-parameters when only MLG-1 placed and biased.

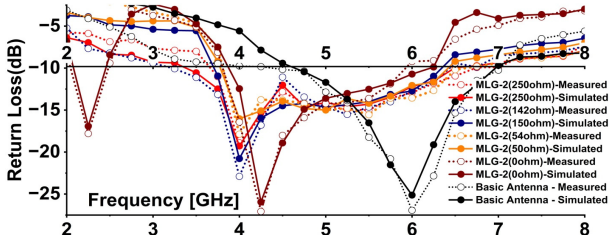

FIGURE 12. Simulated and measured S-parameters when only MLG-2 placed and biased.

current, while varactor diodes exhibit low P1dB and higher intermodulation distortion due to nonlinear capacitance-voltage characteristics. The quasi-ohmic behavior of the graphene pads enables higher power handling and reduced distortion, making them suitable for tunable antenna applications.

To evaluate repeatability and long-term stability, measurements were repeated on the same sample after approximately four months under ambient laboratory conditions. The results in Figure 9(b) show no significant deviation, remaining within measurement uncertainty, indicating good stability of the drop-cast MLG pads against oxidation and environmental variations.

4. EXPERIMENTAL SETUP FOR ANTENNA CHARACTERIZATION

The antenna is characterized using a vector network analyzer (VNA) by exciting the ports with a 50 Ω load impedance. Radiation characteristics are measured in an anechoic chamber, as shown in Figure 10.

The measured results indicate that the proposed antenna exhibits an impedance bandwidth ($S_{11} < -10$ dB) from 2.75 GHz to 6.75 GHz.

When the graphene pad corresponding to MLG-1 is biased from 0 to 6 V, its resistance decreases from approximately 250 Ω to 68 Ω, introducing controlled attenuation and modifying the antenna impedance. This does not produce a significant frequency shift; instead, it results in a progressive narrowing of the operating bandwidth, as observed in the simulated and measured S-parameter responses in Figure 11.

In contrast, biasing MLG-2 produces variable attenuation that shifts the operating band toward lower frequencies. To examine the limiting case, a copper plate is inserted between the patch and the parasitic element, representing an effective zero-ohm condition. The corresponding responses are shown in Figure 12.

To analyze the combined effect, both graphene pads are considered simultaneously. In the first case, the resistance of MLG-1 is fixed at 250 Ω while MLG-2 is varied (150 Ω, 100 Ω,

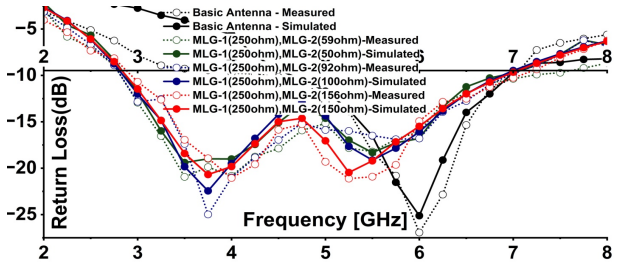

FIGURE 13. Simulated and measured S-parameters when MLG-1 and MLG-2 placed and only MLG-2 biased.

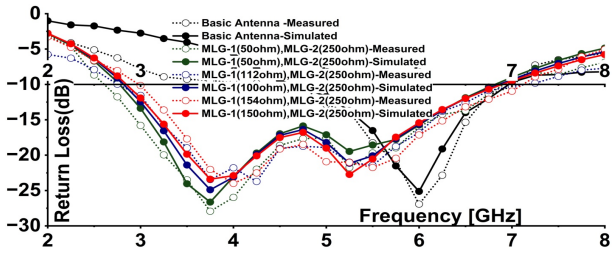

FIGURE 14. Simulated and measured S-parameters when MLG-1 and MLG-2 placed and only MLG-1 biased.

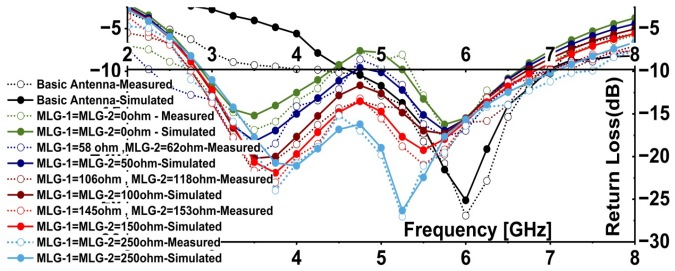

FIGURE 15. Simulated and measured S-parameters when MLG-1 and MLG-2 placed and biased equally.

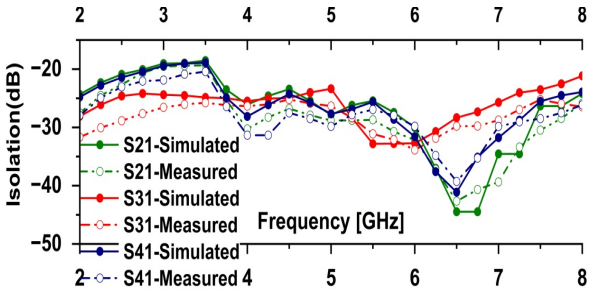

FIGURE 16. Comparison of simulated and measured isolation characteristics of the antenna configuration.

and 50 Ω), resulting in a progressive extension of the operating band toward lower frequencies (2.8 GHz–7.0 GHz), as shown in Figure 13. A similar trend is observed when MLG-2 is fixed, and MLG-1 is varied, confirming their reciprocal influence. However, due to asymmetric placement, MLG-1 mainly affects the resonance near 5.5 GHz, whereas MLG-2 influences the lower-frequency resonance around 3.75 GHz as shown in Figure 14.

In the third case, the two graphene pad resistances are varied simultaneously from 250 Ω to 0 Ω. This results in the formation of a bias-controlled tunable notch band in the 4.8 GHz–5.25 GHz range, where the notch frequency and depth depend on the graphene resistance, as shown in Figure 15. This demonstrates that the proposed design enables both frequency tunability and controllable notch-band characteristics, enhancing its suitability for adaptive and interference-mitigation applications.

The small deviation between simulated and measured results is attributed to fabrication tolerances and measurement uncertainties. Minor variations in graphene pad placement, SMA connector soldering, and cable losses during measurement may contribute to these differences. Nevertheless, the deviation remains within acceptable limits, demonstrating the robustness of the proposed antenna design.

4.1. Isolation Analysis

To enhance mutual isolation, the antenna elements are positioned in a mutually orthogonal orientation. The influence of graphene-pad resistance on the antenna characteristics is investigated by varying the resistance values, where each resistance case is validated using one antenna within the MIMO configuration. For every arrangement, the mutual coupling between the antenna elements is carefully evaluated, and the corresponding isolation characteristics are presented in Figure 16. The worst-case isolation is observed at the minimum resistance of the graphene pads,which was < -20 dB, whereas all other resistance conditions exhibited improved isolation performance. These results confirm that the proposed diagonal antenna arrangement, without any additional decoupling structures, maintains good isolation and does not significantly affect the individual antenna characteristics.

4.2. Peak Gain and Radiation Efficiency

The variations in the simulated and experimentally obtained peak gains of the proposed antenna over the operational frequency range are depicted in Figure 17(a). The results indicate stable radiation performance across the entire band, with the peak gain reaching a maximum value of 5.5 dBi at 6.5 GHz.

In addition, Figure 17(b) illustrates the simulated and measured radiation efficiency characteristics, demonstrating that the antenna maintains high efficiency levels ranging from 80% to 95% throughout the operating band.

4.3. Radiation Pattern

The radiation characteristics of the proposed antenna were evaluated through both simulations and experimental measurements, as depicted in Figures 18(a) and (b) for the E-plane ($\phi = 0°$) and H-plane ($\phi = 90°$) at 3.75 and 5.25 GHz.

At 3.75 GHz, the antenna exhibited a quasi-omnidirectional radiation behavior, whereas a clearly directional radiation pattern was observed at 5.25 GHz. This transition in the radiation behavior indicates the antenna's capability to support diversity-oriented performance. Furthermore, the strong correlation between the simulated and measured radiation patterns validates the effectiveness and accuracy of the proposed antenna design.

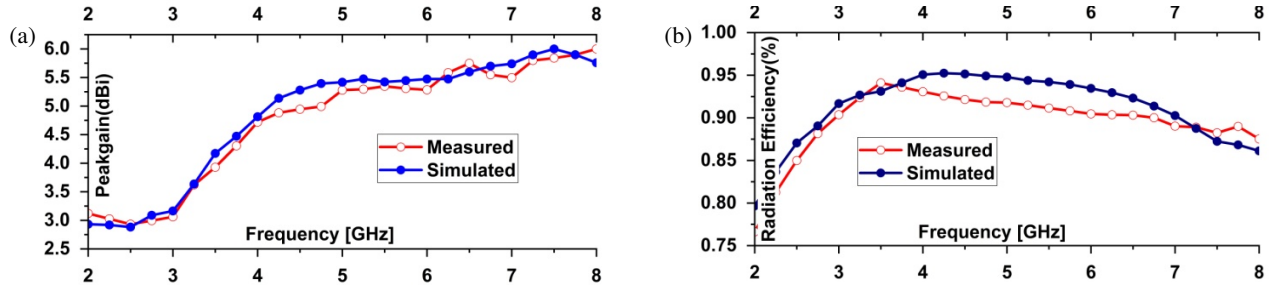

FIGURE 17. Measured and simulated results. (a) Peak gain and (b) radiation efficiency.

TABLE 3. Performance comparison of the proposed antenna with previously reported designs.

Refs.	Original Bandwidth	Tuning Elements	Size of Tuning Elements	Gain (dBi)	R.E (%)	Tuning/Reconfigurable Parameter	Tuning/Reconfigurable Range
[6]	3.5–3.56 GHz 3.65–3.75 GHz	4 — M.S	N/A	13.3–14 dBi	91–95	Frequency tunable	3.4–3.5 GHz
[8]	3.56–3.64 GHz 5.75–5.83 GHz	5 — P.D	N/A	1.1–5.8 dBi	70–86	Pattern tunable	0 to 30°
[11]	2.45–2.77 GHz	4 — P.D	N/A	4–6.1 dBi	45–55	Frequency tunable	2.3–3.04 GHz
						Pattern reconfigurable	−30°–+30°
[13]	0.5–1 GHz 1.2–1.78 GHz	18 — V.D	N/A	N/A	N/A	Frequency tunable	0.485–1.78 GHz
[23]	R.F.1 — 1.315 GHz R.F.2 — 2.315 GHz	2 — G.P	$5.15 \times 10\,mm^2$	N/A	N/A	Frequency tunable	1.25–1.5 GHz 2.25–2.5 GHz
[24]	R.F.1 — 2.41 GHz R.F.2 — 3.45 GHz	2 — G.P	$0.65 \times 1\,mm^2$ $1.2 \times 1\,mm^2$	N/A	N/A	Frequency tunable	2.45–2.6 GHz 3.3–3.6 GHz
[25]	0.68 THz–0.72 THz (Only Simulated Results)	7 — G.P	1, 2 — $55 \times 55\,\mu m^2$ 3, 5 — $76 \times 76\,\mu m^2$ 4 — $81 \times 81\,\mu m^2$ 6, 7 — $60 \times 60\,\mu m^2$	1.3–3.6 dBi	45–58	Frequency tunable	0.77–0.8 THz 0.88–0.92 THz
[26]	6.5–7.4 GHz	2 — G.P	$1 \times 0.3\,mm^2$ $0.81 \times 0.3\,mm^2$	N/A	N/A	N/A	5.6–7.9 GHz
P.W	4.8–7 GHz	2 — G.P	$1 \times 2.5\,mm^2$ $0.85 \times 2\,mm^2$	3–5.5 dBi	80–95	Frequency tunable	2.75–6.75 GHz

* Refs. — References, R.E — Radiation efficiency, M.S — Metal Screws, P.D — PIN Diode, V.D — Varactor Diode, G.P — Graphene Pad, P.W — Proposed Work, R.F — Resonant Frequency, N/A — Not available

4.4. Performance Comparison

A comparative analysis of recently reported frequency-tunable antennas, highlighting the tuning range, tuning mechanisms, physical size of the tuning elements, gain, and radiation efficiency, is presented in Table 3.

4.5. Diversity Performance

The level of interaction between antenna elements in a multi-element configuration is commonly assessed using the envelope correlation coefficient (ECC). For a MIMO system to perform effectively, the ECC value should remain low, typically below 0.5. The diversity gain (DG), which reflects the ability of the antenna system to mitigate fading, remains close to 10 dB for the proposed antenna system.

Figure 19(a) presents the ECC calculated from both simulated and measured S-parameters. Across the operating frequency band, the ECC remained below 0.02. Figure 19(b) shows that the DG consistently exceeds 9.97, indicating excellent diversity performance.

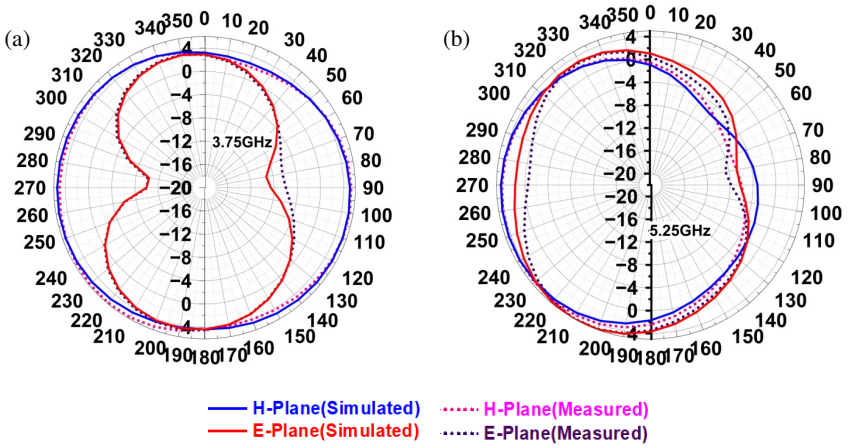

FIGURE 18. Measured and simulated radiation patterns at (a) 3.75 GHz, (b) 5.25 GHz.

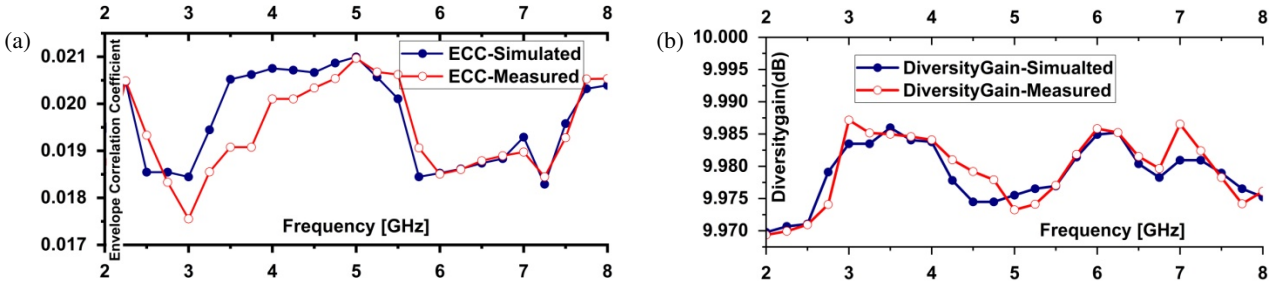

FIGURE 19. Simulated and measured (a) envelope correlation coefficients, (b) diversity gains.

5. CONCLUSIONS

This work presents a compact approach for achieving frequency reconfigurability and controllable notch characteristics in a wideband microstrip antenna operating from 2.75 GHz to 6.75 GHz. By employing bias-controlled multilayer graphene pads, the antenna response is effectively tuned through resistance variation without increasing system complexity. The asymmetric placement of graphene pads enables selective control of resonant modes, while their combined operation produces a tunable notch band in the 4.8 GHz–5.25 GHz range. The proposed configuration maintains stable MIMO performance with good agreement between simulated and measured results. Overall, the design offers a low-complexity and flexible solution for adaptive and interference-resilient sub-6 GHz wireless communication systems.

Future work will focus on integrating on-substrate bias circuitry and exploring graphene inkjet printing for scalable fabrication. Hybrid tuning using graphene pads with varactor diodes will be investigated for a wider tuning range and improved linearity. Additionally, emerging materials, such as MXene and black phosphorus, and real-world deployment aspects across sub-6 GHz applications will be explored.

REFERENCES

[1] Hu, J., X. Yang, L. Ge, Z. Guo, Z.-C. Hao, and H. Wong, "A reconfigurable 1×4 circularly polarized patch array antenna with frequency, radiation pattern, and polarization agility," *IEEE Transactions on Antennas and Propagation*, Vol. 69, No. 8, 5124–5129, Aug. 2021.

[2] Subhi, K., F. C. Seman, S. A. Hamzah, G. C. Hock, and S. M. Shah, "Circuit model for microstrip array antenna with defected ground structures for mutual coupling reduction and beamforming applications," *International Journal of Integrated Engineering*, Vol. 13, No. 1, 101–119, 2021.

[3] Darvazehban, A., S. A. Rezaeieh, O. Manoochehri, and A. M. Abbosh, "Two-dimensional pattern-reconfigurable cross-slot antenna with inductive reflector for electromagnetic torso imaging," *IEEE Transactions on Antennas and Propagation*, Vol. 68, No. 2, 703–711, 2020.

[4] Ahmad, K. S. and M. Z. A. A. Aziz, "Pattern reconfigurable planar antenna array based on two circular defected ground structure," *Przegląd Elektrotechniczny*, Vol. 97, No. 7, 52–55, 2021.

[5] Elabdi, A., M. El Ayachi, M. Rahmoun, and A. Lamkaddem, "A review of reconfigurable antenna types and mechanisms for wireless communications: IoT applications," in *2025 International Conference on Circuit, Systems and Communication (ICCSC)*, 1–8, Fez, Morocco, 2025.

[6] Chen, R.-S., X.-D. Li, H.-L. Liu, G.-L. Huang, S.-W. Wong, M. K. T. Al-Nuaimi, K.-W. Tam, and W.-W. Choi, "Reconfigurable full-metal circularly-polarized cavity-backed slot antenna and array with frequency and polarization agility," *IEEE Transactions on Circuits and Systems II: Express Briefs*, Vol. 70, No. 2, 531–535, Feb. 2023.

[7] Babakhani, B., S. K. Sharma, and N. R. Labadie, "A frequency agile microstrip patch phased array antenna with polarization reconfiguration," *IEEE Transactions on Antennas and Propagation*, Vol. 64, No. 10, 4316–4327, Oct. 2016.

[8] Selvam, Y. P., M. G. N. Alsath, M. Kanagasabai, L. Elumalai, S. K. Palaniswamy, S. Subbaraj, S. Kingsly, G. Konganathan, and I. Kulandhaisamy, "A patch-slot antenna array with compound reconfiguration," *IEEE Antennas and Wireless Propagation Letters*, Vol. 17, No. 3, 525–528, Mar. 2018.

[9] Mu, Y., J. Han, D. Xia, and X. Ma, "Electronically steerable parasitic patches for dual-polarization reconfigurable antenna using varactors," *The Applied Computational Electromagnetics Society Journal (ACES)*, Vol. 37, No. 1, May 2022.

[10] Wu, J., X. Lu, W. Wang, J. Han, G. Xu, and Z. Huang, "Design of a compact polarization-agile and frequency-tailored array antenna with digital-controllable radiation beams," *IEEE Transactions on Antennas and Propagation*, Vol. 70, No. 2, 813–822, Feb. 2022.

[11] Rodrigo, D., B. A. Cetiner, and L. Jofre, "Frequency, radiation pattern and polarization reconfigurable antenna using a parasitic pixel layer," *IEEE Transactions on Antennas and Propagation*, Vol. 62, No. 6, 3422–3427, Jun. 2014.

[12] Bharambe, V. T., J. Ma, M. D. Dickey, and J. J. Adams, "RESHAPE: A liquid metal-based reshapable aperture for compound frequency, pattern, and polarization reconfiguration," *IEEE Transactions on Antennas and Propagation*, Vol. 69, No. 5, 2581–2594, May 2021.

[13] Xu, J. and Y. Zhu, "Tunable bandpass filter using a switched tunable diplexer technique," *IEEE Transactions on Industrial Electronics*, Vol. 64, No. 4, 3118–3126, 2017.

[14] Xu, J., "A tunable diplexer based on mixed coupling varactor-tuned stepped-impedance resonators," *Microwave and Optical Technology Letters*, Vol. 58, No. 6, 1469–1473, 2016.

[15] Ghivela, G. C. and J. Sengupta, "The promise of graphene: A survey of microwave devices based on graphene," *IEEE Microwave Magazine*, Vol. 21, No. 2, 48–65, 2020.

[16] Wu, B., C. Fan, X. Feng, Y.-T. Zhao, J. Ning, D. Wang, and T. Su, "Dynamically tunable filtering attenuator based on graphene integrated microstrip resonators," *IEEE Transactions on Microwave Theory and Techniques*, Vol. 68, No. 12, 5270–5278, 2020.

[17] Zhang, A.-Q., W.-B. Lu, Z.-G. Liu, B. Wu, and H. Chen, "Flexible and dynamically tunable attenuator based on spoof surface plasmon polaritons waveguide loaded with graphene," *IEEE Transactions on Antennas and Propagation*, Vol. 67, No. 8, 5582–5589, 2019.

[18] Wu, B., H.-R. Zu, B.-Y. Xue, Y.-T. Zhao, and Q. S. Cheng, "Flexible wideband power divider with high isolation incorporating spoof surface plasmon polaritons transition with graphene flake," *Applied Physics Express*, Vol. 12, No. 2, 022008, 2019.

[19] Zu, H.-R., B. Wu, Y.-H. Zhang, Y.-T. Zhao, R.-G. Song, and D.-P. He, "Circularly polarized wearable antenna with low profile and low specific absorption rate using highly conductive graphene film," *IEEE Antennas and Wireless Propagation Letters*, Vol. 19, No. 12, 2354–2358, 2020.

[20] Fan, C., B. Wu, Y. Hu, Y. Zhao, and T. Su, "Millimeter-wave pattern reconfigurable Vivaldi antenna using tunable resistor based on graphene," *IEEE Transactions on Antennas and Propagation*, Vol. 68, No. 6, 4939–4943, Jun. 2020.

[21] Zhang, J., Z. Li, L. Shao, and W. Zhu, "Dynamical absorption manipulation in a graphene-based optically transparent and flexible metasurface," *Carbon*, Vol. 176, 374–382, 2021.

[22] Huang, C., B. Zhao, J. Song, C. Guan, and X. Luo, "Active transmission/absorption frequency selective surface with dynamical modulation of amplitude," *IEEE Transactions on Antennas and Propagation*, Vol. 69, No. 6, 3593–3598, 2021.

[23] Chen, J., S. Zhu, L. Li, and C. Fan, "Microstrip bandpass diplexer with linear-tunable attenuation based on graphene flakes," *Materials Letters*, Vol. 316, 132059, 2022.

[24] Akkapanthula, S. H. and S. Kagita, "Tunable attenuating diplexer using miniaturized multilayer graphene pads," *International Journal of Microwave and Wireless Technologies*, Vol. 16, No. 10, 1722–1729, 2024.

[25] Ahmad, K. S. and A. J. A. Al-Gburi, "Graphene-based frequency reconfigurable slot antenna for terahertz applications," *Optik*, Vol. 330, 172343, 2025.

[26] Ullah, S. and M. Yasir, "Amplitude and phase control in SIW structures by tuning multilayered graphene," *Scientific Reports*, Vol. 15, No. 1, 38456, 2025.

[27] Ta, S. X., "A dual-band dual-sense circularly polarized patch antenna using hybrid capacitive-inductive proximity-coupling feed," *AEU — International Journal of Electronics and Communications*, Vol. 184, 155408, 2024.

[28] Wichaidit, P., S. Dentri, P. Janpangngern, T. Lertwiriyaprapa, M. Krairiksh, and C. Phongcharoenpanich, "Broadband CP corner-truncated microstrip antenna with irregularly hexagonal AMC for 2.45 GHz applications," *Alexandria Engineering Journal*, Vol. 97, 88–99, 2024.

[29] Nguyen-Huy, H., D.-N. Tran-Viet, P. Kim-Thi, and H. Tran-Huy, "Compact high-gain circularly polarized patch antenna based on TM_{30}/TM_{03} mode," *PLoS One*, Vol. 20, No. 5, e0321091, May 2025.

[30] Pozar, D. M., *Microwave Engineering*, 4th ed., John Wiley & Sons, 2011.

[31] Balanis, C. A., *Antenna Theory: Analysis and Design*, 4th ed., John Wiley & Sons, 2016.

[32] Garg, R., P. Bhartia, I. Bahl, and A. Ittipiboon, *Microstrip Antenna Design Handbook*, Artech House, 2001.

[33] Amari, S., U. Rosenberg, and J. Bornemann, "Adaptive synthesis and design of resonator filters with source/load-multiresonator coupling," *IEEE Transactions on Microwave Theory and Techniques*, Vol. 50, No. 8, 1969–1978, Aug. 2002.

[34] Hammerstad, E. and O. Jensen, "Accurate models for microstrip computer-aided design," in *1980 IEEE MTT-S International Microwave symposium Digest*, 407–409, Washington, DC, USA, 1980.

[35] Gupta, K. C., *et al.*, *Microstrip Lines and Slotlines*, Artech House, 1996.

[36] Hong, J.-S. and M. J. Lancaster, *Microstrip Filters for RF/Microwave Applications*, John Wiley & Sons, 2001.

[37] Mandal, S., S. K. Mandal, A. K. Mal, and R. Mahapatra, "A UWB dual band-notched on-chip antenna and its equivalent circuit model," *Progress In Electromagnetics Research B*, Vol. 97, 19–35, 2022.

[38] Lee, D.-H., H.-Y. Yang, and Y.-K. Cho, "Design and analysis of tapered slot antenna with 3.5/5.5 GHz band-notched characteristics," *Progress In Electromagnetics Research B*, Vol. 56, 347–363, 2013.